SYNTHESIS AND CHARACTERIZATION OF CD³⁺ DOPED LITHIUM FERRITE (LCF) BY SOL-GEL AUTO-COMBUSTION

Chetan Suryakant Shinde Department of Applied Sciences and Humanities, Gharda Institute of Technology, Lavel, Khed-410203, Maharashtra, India Email- chetann.shinde@gmail.com
Nitin Devram Sali Department of Electronic Science, Padmashri Vikhe Patil college of Arts, Science and Commerce, Pravaranagar, Loni-413713, Rahata, Ahmednagar, Maharashtra, India Email-snitind7@gmail.com

Abstract:
In this study, we pursued an alternative approach, noteworthy departure from traditional methods, paving the way for successful synthesis of Nanocrystalline $Li_{1-x}Cd_xFe_2O_4$ (where x = 0, 0.1, 0.2, 0.3, 0.4) using the sol-gel auto-combustion method with citrate-nitrate precursors. The structural parameters were effectively investigated using X-ray Diffraction (XRD) and Field Emission Scanning Electron Microscopy (FE-SEM), which showed a single cubic spinel phase for all the samples. It was observed that the lattice parameter increased, and the crystallite size of the spinel decreased as the Cadmium content increased in lithium ferrite. Additionally, Vibration Sample Magnetometry (VSM) was used to identify a complex magnetic structure with significant changes in the heated sample. The indirect energy band gap was evaluated using the TAUC plot for all samples, which showed an increase from 2.17 to 3.39 eV by increasing Cd content. It was further discovered that the energy band gap was a function of crystallite size. Finally, FTIR was used to confirm the spinel nature of the Ferrite Nanomaterial, having characteristic absorption peaks at 588 and 435 cm^{-1}. TEM images showed the shape of the LCF nanoparticles to be approximately spherical with particle size well-matched with the crystallite size obtained from the XRD.
Keywords: sol-gel auto-combustion, Spinel ferrite, VSM, XRD, WH plot

1.Introduction:

Nanotechnology is a rapidly growing field of research with immense potential in the fields of electronics and medicine. It involves manipulating and engineering materials ranging from 1-100 nm in size . Nanoparticles are microscopic objects possessing unique properties that depend on their size due to their relatively larger surface area. Since particles at the nanoscale are smaller than the wavelength of light or the de Broglie wavelength of the charge carrier, they exhibit different physical properties compared to bulk materials [2]. This opens up new and exciting possibilities for their application. Ferrites are an amazing class of materials that have found a wide range of applications such as in permanent magnets, high-density storage devices, and targeted drug delivery [3]. Interestingly, the substitution of magnetic or non-magnetic cations significantly affects the cationic distribution on A and B sites, thereby influencing the magnetic interactions and magnetic properties [4]. Recently, spinel ferrite nanoparticles have been the subject of significant interest due to their unique properties and potential uses in various fields such as catalysis [5], sensors [6], electrodes [7], adsorption [8], batteries [9], supercapacitors [10], etc. The spinel ferrite nanoparticles are made up of ions of metals, A^{2+} and B^{3+}, which can be found in either tetrahedral or octahedral sites, and an anion, typically O^{2-} [11], with oxygen anions occupying face-centered cubic positions. One of the most exciting features of spinel ferrite nanoparticles is their distinct optical, electronic, and magnetic properties that make them highly permeable, with good saturation magnetization and no preferred direction of magnetization. Additionally, these nanoparticles are magnetically "soft," meaning they can be easily magnetized and demagnetized, and are electrically insulating. For these reasons, ferrites have been used as magnetic, refractory, and catalysts [12]. Furthermore, magnetic iron oxide nanoparticles are currently being researched due to their potential applications in bio-sensing [13], ferrofluids [14], data storage [15], drug delivery system [16], magnetic resonance imaging [17], optical devices [18], etc. Lithium ferrite is an exceptional type of ferrimagnetic oxide that belongs to a group

of oxides called spinel. It is highly regarded for its numerous desirable properties, such as square hysteresis loop characteristics with high saturation magnetization, high-value Curie temperature, and microwave dielectric losses is low [19]. When combined with lithium in electronic devices, the conductivity can be further increased, resulting in maximum conduction, also storage capacity, as well as a high charging and low discharging rate. Due to its wide range of technological applications in devices of microwave and magnetic recording tapes, transformer cores and other electronic applications. Lithium ferrite has gained considerable attention and is widely considered a promising candidate for electrode material in rechargeable lithium-ion batteries and supercapacitors [20]. Its importance in construction and engineering makes it a valuable and promising material for a variety of applications [21]. The substitution of Cadmium (Cd) in lithium ferrite ($LiFe_2O_4$) is a widely used technique that enhances the magnetic properties of the material, particularly the saturation magnetization. This process involves replacing some of the iron (Fe) ions in the crystal lattice of lithium ferrite with cadmium ions, which results in the improvement of the material's magnetic performance. Lithium ferrite is a type of magnetic material that consists of lithium ions (Li^+) occupying tetrahedral sites and iron ions (Fe^{3+}) occupying octahedral sites in the crystal structure. The specific effects of cadmium substitution on the material are dependent on the concentration of cadmium ions and the sites in the crystal lattice where the substitution occurs [22]. In short, Cd^{3+} ions preferentially occupy the A-site, pushing Fe^{3+} to the B-site, resulting in an increased magnetic moment [23]. Hence, the addition of Cd^{3+} ions allows for the adjustment of magnetic properties. The production and synthesis of nanoparticles have advanced significantly in recent years, with various methods available for this process such as the sol-gel auto-combustion method, hydrothermal method, mechanical alloying method, solvothermal method, vapor phase compression method, plasma method, and electrochemical methods. While all of these methods hold promise, the sol-gel auto-combustion method stands out due to its popularity and wide industrial application. The sol-gel auto-combustion technique is a particularly fast and cost-effective method for creating particulate products, including various metal and alloy nanoparticles. This technique allows for the mixing of different elements at the atomic level, resulting in the formation of nano-sized, homogeneous, and highly reactive powders that can be utilized in a variety of applications, capable of producing high-quality ferrite nanoparticles in the same size on an industrial scale. [24-29]. The sol-gel method is an immensely powerful technique that offers a host of benefits. It is capable of producing highly homogeneous composites with exceptional purity levels of up to 99.99 %, making it a popular choice for synthesizing ferrites. One of the biggest advantages of this method is that it operates at lower temperatures between 70 and 320 °C, which allows for the production of uniform nanostructures and helps to streamline the manufacturing process. Additionally, the sol-gel process yields products with high purity levels, narrow particle size distribution, and low-temperature uniformity. Overall, the sol-gel technique is a reliable and effective method for creating high-quality metal and ceramic nanomaterials, requiring low temperature and less external energy as compared to the traditional methods, resulting in a shorter processing time. [30-31]. Here, from this method, size, morphology and the surface area of the obtain ferrite material can changed by varying the annealing temperature [32-34]. Tsering Namgyal and co-researchers synthesized lithium ferrite by sol-gel auto-combustion method. The α-form has a space group of P_1^{332}, while the disordered β-form has a space group of Fd_3m. The γ- and δ-phases are stable with temperature, making them suitable for various applications such as lithium-ion batteries, supercapacitors and other energy storage devices. Unlike the α- and β-phases, the γ- and δ-phases do not undergo phase transition, and this makes them more desirable for certain applications [35]. Hu Yang et. al explored the innovative doping of $Cd_xNi_{0.5−x}Cu_{0.2}Zn_{0.3}Fe_2O_4$ ($0 \leq x \leq 0.50$) spinel ferrite with divalent excess metal particles (Cd^{2+}) and its impact on the lattice structure was prepared using the sol-gel method. Additionally, the study highlighted the effects of Cd^{2+} doping on the morphology, magnetic properties, and dielectric properties of Ni-Cu-Zn spinel ferrite, due to the large radius of cadmium ions and their preference for a tetrahedral environment. The findings suggest that the use of isolator-doped Ni-Cu-Zn spinel ferrite could be a promising area of interest for future research [36].

Recent research has shown that lithium ferrite and vanadium-doped lithium ferrite by sol-gel process, have great potential for use in a variety of applications such as thermochromic materials, optoelectronic devices, and as a cathode material for rechargeable lithium batteries mentioned by S. Malathi and collogues. The VSM results indicate that these materials exhibit superparamagnetic behavior, which suggests that they can be utilized to create several useful applications such as pigments, sensors, electronics devices, recording materials, and other innovative technologies [37]. P. Hajasharif and team's research on copper-doped lithium ferrite nanoparticles synthesized using the sol-gel technique is a significant step forward. By providing a low-cost alternative to the more expensive garnet materials used in microwave applications in the industry, lithium ferrite nanoparticle is proving to be a promising and widely used magnetic material. Additionally, its potential for use as cathode materials in rechargeable lithium-ion batteries adds to its already impressive versatility. They use of the sol-gel method in preparing the copper-doped lithium ferrite $Cu_xLi_{1-x}Fe_2O_4$ (x=0.2) ferrite nanocomposite, followed by calcination at 700 $°C$, is commendable. The magnetic measurement of the copper-doped lithium ferrite nanocomposite also provides valuable insights into the nature of its low coercivity, which is due to the presence of a paramagnetic nature [38]. The study conducted by Vivek Verma et al. on substituted lithium ferrites using the solid-state technique highlights the possibility of improving the properties of ferrite samples for microwave devices. The research shows that a small amount of Fe content can enhance the permeability and reduce the power loss of cadmium-doped lithium ferrites as compared to zinc-doped lithium ferrites. This could be a valuable insight towards the development of advanced microwave devices [39]. In the present study, the synthesis of Lithium ferrite with cadmium doped (LCF) using the sol-gel auto-combustion method is a promising development in the field of electronics applications like batteries and supercapacitors. LCF's high energy density and long lifespan make it an attractive option for these applications [40]. To achieve optimal results, it is important to use an appropriate synthesis method for the formation of the spinel phase. Substituted lithium ferrites are particularly advantageous as they can be applied in the microwave frequency range. It is worth noting that sintering is essential for the formation of the spinel phase, as well as for improving crystallinity and achieving equilibrium cationic distribution. However, due to the low melting point of both lithium and cadmium, high-temperature sintering cannot be used without affecting stoichiometry due to Li evaporation. X-ray diffraction (XRD) was used to study the structural properties of the powders, and the Scherer formula was applied to obtain a minimum crystallite size of 11 nm, which correlated with the WH plot. The effect of Cd^{3+} substitution on the magnetic properties of lithium ferrites was evaluated using M-H curves at room temperature. In addition, the synthesized LCF was analyzed using FT-IR, UV-Vis, and FE-SEM to obtain a comprehensive understanding of its properties. Overall, this development is promising, and further research could lead to significant advancements in the field of electronic applications. The main aim of the present work is to enhance the electric and magnetic properties of Lithium ferrite by doping cadmium with different concentrations, which is useful in energy storage devices in future.

2. Experimental methods and materials:

The lithium ferrite doped with Cd^{3+} and having the compositional formula $Li_{1-x}Cd_xFe_2O_4$ (LCF) at x=0, 0.1, 0.2, 0.3, 0.4 was prepared using the sol-gel auto-combustion method. The starting materials, used for the synthesis with high-purity AR grade ferric nitrate $[Fe(NO_3)_3.9H_2O]$, cadmium nitrate $[Cd(NO_3)_2.6H_2O]$, citric acid $[C_6H_8O_7]$, and ammonium hydroxide solution $[NH_4\text{-}OH]$ were collected from Merck chemical company in India. The nitrates and citric acid were mixed in a stoichiometric ratio of 1:3 and dissolved separately in a minimum amount of deionized water to obtain clear aqueous solutions. The solutions were then mixed and stirred continuously to achieve a homogeneous solution. Gradually, 30 % ammonium hydroxide solution was added to set the pH of the solution at 7. The solution was heated steadily at 100 °C, which converted it into a thick gel. The gel was then dried, and the complete evaporation of water molecules caused it to self-ignite and form fine

ash. Finally, the ash was mixed in a mortar to obtain a homogeneous powder. The detailed flowchart of the synthesis process is given in Fig. 1.

Figure 1. Flow-chart for the synthesis of $Li_{1-x}Cd_xFe_2O_4$ (LCF) at x=0, 0.1, 0.2, 0.3, 0.4
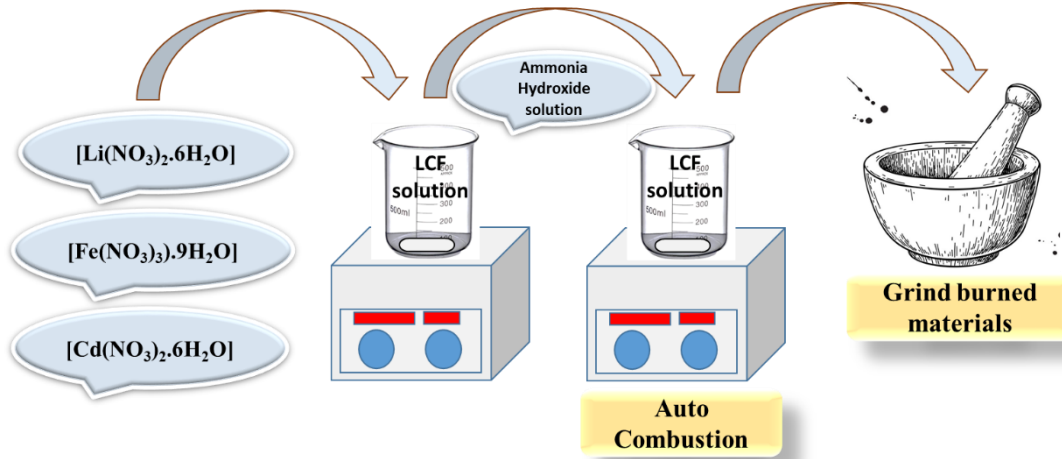
3. Results and discussion:

3.1. XRD Analysis:

Conducting a structural study is crucial to optimize the properties required for different applications. In this study, X-ray diffractometer was used to perform phase identification and determine the lattice constant along with other structural parameters [41]. Fig. 2A displays the X-ray diffraction patterns for the LCF with x = 0.0 to 0.4 ferrite that were sintered at 600 °C for 5 hours. Upon analyzing the XRD patterns, it is evident that the position of the peaks is following the reported values of Li-Cd [42]. The observed peaks at (220), (311), (222), (400), (422), (511), (440), and (533) confirm the spinel structure of the LCF, which perfectly matches with the [43]. This study provides valuable insights into optimizing the properties of the LCF for various applications. The ferrite compositions synthesized in this study exhibit a single-phase cubic spinel structure with no ambiguous reflections, indicating the homogeneity of the prepared LCF. Analysis of this confirms the presence of a single-phase cubic spinel structure, with the (311) peak being the most intense [44]. Here, further investigated the structural properties and extracted various parameters such as crystalline size (D_p), lattice parameter, dislocation line density, and X-ray density from the XRD micrograph using the (311) peak, as shown in Table 1. The size of the crystallite was calculated, denoted as "D_p", using Scherrer's formula (equation 1) [45]. These findings provide valuable insights into the structural properties of the synthesized ferrite compositions.

$$D_p = \frac{K\lambda}{\beta cos\theta} \dots \dots \dots \dots \dots \dots \dots \dots \dots \dots \dots (1)$$

Where, D_p=Crystallite size

K= Scherrer's constant (K=0.94)

The crystallite size range of the LCF was found to be between 11.13 and 32.79 nm, as the amount of Cd^{3+} was increased. The difference in the ionic radii of Cd^{3+} (1.03 Å) and Li^{1+} (0.74 Å) caused variations in the diffraction pattern, which led to the variation in the crystallite size, shown in Fig. 3A. The LCF structure consists of Fe^{3+} ions in tetrahedral and octahedral sites and Li^{1+} ions [46]. Adding Cd^{3+} ions to maintain these charges causes Li^{1+} ions to shift to different sites. However, the larger ionic radius of Cd^{3+} ions distorts the crystal lattice, not allowing smaller Li^{1+} ions to fit perfectly in the lattice. These distortions in crystal lattice change the lattice plane space, resulting in changes in the crystal size of LCF. The addition of Cd^{3+} to Lithium ferrite causes the substitution of the Cd^{3+} ions for the Li ions. When lithium ions move from one site to another in a crystal lattice, it can impact the arrangement of atoms and alter the symmetry of the lattice, which can then affect the size of the crystallites. If the lithium ions shift to octahedral sites, the arrangement may become more compact

and result in smaller crystallites [47]. Conversely, if they move to tetrahedral sites, the arrangement may become less compact and result in larger crystallites. The movement of lithium ions in lithium ferrite from tetrahedral to octahedral or vice versa due to cadmium addition can influence the size of the crystallites by changing the lattice structure. The specific impact on the size of the crystallites will depend on the degree of ion substitution and the resulting lattice distortions that occur due to the difference in ionic radii between Cd and Li ions [48].

The study aimed to determine the distance between different crystal planes by analyzing the X-ray diffraction pattern. The intensity versus the 2θ graph was used along with Bragg's law to calculate the values. The Table provides the lattice constant, calculated using formula 3. It was found that the LCF belongs to cubic spinel without any deviation from the ideal d-spacing values, indicating the absence of the tetragonal phase [49]. Each peak was assigned plane indices (hkl). Upon increasing Cd^{3+} ions, the interplanar spacing and lattice constant of LCF increased from 2.506 to 2.528 and 8.3143 to 8.3869 Å, respectively. The Fig. 2B illustrates the variation of interplanar distance and lattice constant with Cd^{3+} ions. The larger ionic radii of Cd^{3+} ions replace Fe^{3+} ions with smaller ionic radii, causing an expansion of the unit cell due to increased lattice parameters [50]. The inter-planar spacing of different crystal planes has been obtained from the intensity versus 2θ graph of the X-ray diffraction pattern using Bragg's law equation 2 [51],

$$d = \frac{n\lambda}{2sin\theta} \dots\dots\dots\dots\dots\dots\dots\dots\dots\dots\dots\dots\dots\dots\dots\dots (2)$$

$$a = d\sqrt{(h^2 + k^2 + l^2)} \dots\dots\dots\dots\dots\dots\dots\dots\dots\dots\dots (3)$$

λ=X-ray Wavelength (1.54 A^0)

B=Full width at half maximum (FWHM) of the peak and

θ=Bragg angle

a=Lattice constant

d=Interplanar distance

The cell volume of the LCF was determined by using different lattice constant values, ranging from 589.9436 to 572.4339 $Å^3$, given in Fig. 4A and a certain amount of Cd^{3+} calculated from equation 4. There is a relationship between the volume and lattice constant, which is expressed in an equation. As the concentration of Cd increases, the X-ray density (formula 5) also increases up to 5.1270 (gm/cc). This indicates that when the lattice parameter decreases, the X-ray density increases. The X-ray density (dx) increases almost linearly with the amount of Cd^{3+} doping, as the larger mass of Cd^{3+} ions replaces the Fe^{3+} ions on the octahedral sites [52] [53]. The fluctuation of X-ray density and lattice constant with cd content is given in Fig. 4B-C.

$$V = a^3 \dots\dots\dots\dots\dots\dots\dots\dots\dots\dots\dots\dots\dots (4)$$

$$d_x = \frac{8M}{Na^3} \dots\dots\dots\dots\dots\dots\dots\dots\dots (5)$$

V=Volume of the unit cell

N=Avogadro's number

M=Molecular weight of the sample

8 = Number of molecules of the spinel lattice for the unit cell

dx=X-ray density.

$$\rho_D = \frac{1}{D^2} \dots\dots\dots\dots\dots\dots\dots\dots\dots\dots\dots\dots\dots (6)$$

$$\varepsilon = \frac{\beta cos\theta}{4} \dots\dots\dots\dots\dots\dots\dots\dots\dots\dots\dots (7)$$

Where ρ_D is dislocation density and ε is microstrain

The Table 1. Presents valuable insights into the effect of Cd^{3+} content on the dislocation density and microstrain of the nanocomposite, calculated from formula 6. The increase in Cd^{3+} content leads to a fluctuation in microstrain values, which is attributed to the impact of grain size on the comprehensive stress of the material, given in Fig. 4D from equation 7. Meanwhile, the number of dislocation lines

per unit area inside the nanocomposite decreases with the increase in crystallite size. The microstrain values increase with Cd^{3+} content, due to the high effect of grain size on the comprehensive stress of the nanocomposite [54]. Dislocations are crystallographic defects that strongly affect material properties, and the dislocation density (D) is a measure of the number of dislocations in a unit volume of a crystalline material. The presented data shows that the dislocation density increases from 0.003511 to 0.031297 line/m^2 with an increase in Cd^{3+} ions, presented in Fig. 3B [55].

Figure 2. A) XRD pattern of $Li_{1-x}Cd_xFe_2O_4$ (LCF) at x=0, 0.1, 0.2, 0.3, 0.4 B) Variation of interplanar distance and lattice constant $Li_{1-x}Cd_xFe_2O_4$ (LCF) with x=0, 0.1, 0.2, 0.3, 0.4
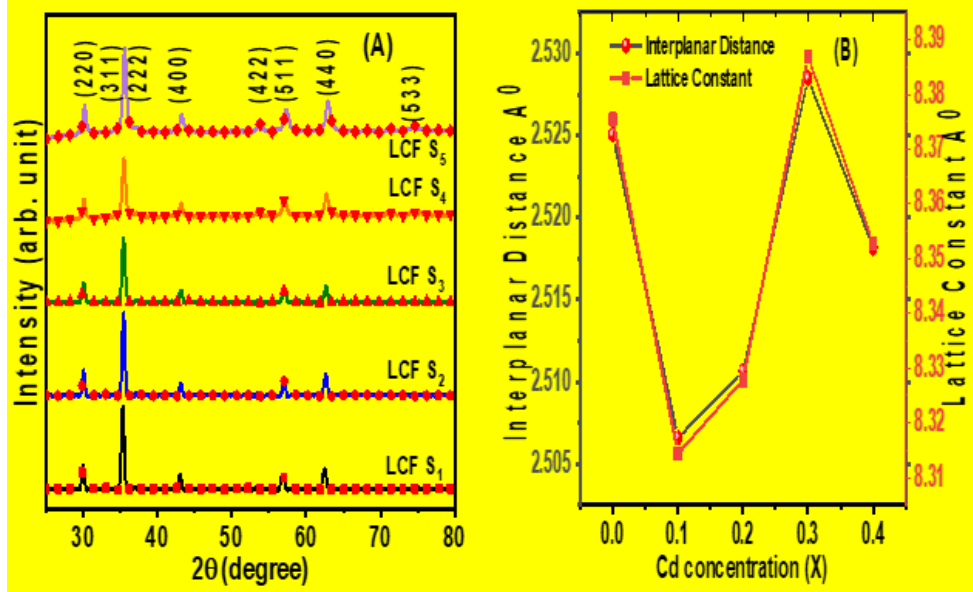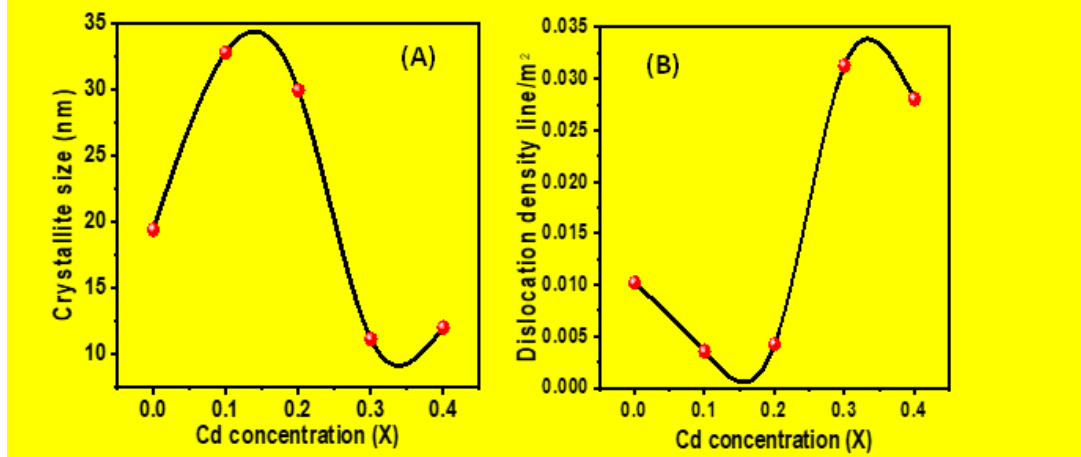

Figure 3. A) Variation of crystallite size of $Li_{1-x}Cd_xFe_2O_4$ (LCF) with x=0, 0.1, 0.2, 0.3, 0.4 B) Variation of Dislocation density

Samples	Crystallite Size (nm)	Lattice Constant (Å)	Cell volume (V) (Å)³	X-Ray Density (gm/cc)	Micro-strain (%)	Dislocation density (line/m²)	Interplanar Distance (Å)
LCF S1	19.41	8.3755	587.534999	4.0926	0.001931	0.010209	**2.525025544**
LCF S2	32.79	8.3143	574.758134	4.4667	0.001113	0.003511	**2.506587699**

LCF S3	29.93	8.3278	577.564348	4.6877	0.001228	0.004235	2.510660487
LCF S4	11.13	8.3869	589.943617	4.8269	0.003399	0.031297	2.528471313
LCF S5	12	8.3527	582.757953	5.1270	0.003273	0.028064	2.51816354

3.2. Hopping and Bond Length:

$$L_A = \frac{\sqrt{3}}{4} a \ldots\ldots\ldots\ldots\ldots\ldots\ldots.\ldots\ldots\ldots\ldots. (8)$$

$$L_B = \frac{\sqrt{2}}{4} a \ldots\ldots\ldots\ldots\ldots\ldots\ldots\ldots\ldots\ldots\ldots (9)$$

The study calculated the hopping lengths for ions in the octahedral site (LB) and the tetrahedral site (LA) using a formula 8 and 9 discussed elsewhere, which increased from 3.6002 to 3.6316 and 2.9399 to 2.9656 respectively, with Cd amount [56]. The results, presented in Fig. 5A and the accompanying Table, show that LA and LB fluctuate as Cd^{3+} content increases. The change is attributed to the variation of the lattice constant in LCF with content Cd^{3+}. The study also found that the magnetic ion interaction at the B-site is less than at the A-site due to the compressive strain caused by migrated Fe^{3+} and oxygen ions [57]. This finding sheds light on the reduction of magnetic interaction in both the tetrahedral sites. The study further suggests that the observed linear increase in the magnetic interaction distance with Cd^{3+} concentration may be due to the tetrahedral occupation of Cd^{3+} and the octahedral occupation of Li^{1+} ion [58]. These findings provide valuable insights into the behavior of ions in octahedral and tetrahedral sites, which could inform the development of new materials with desirable magnetic properties [59].

$$dAX = \left(\mu - \frac{1}{4}\right)\alpha\sqrt{3} \ldots\ldots\ldots\ldots\ldots\ldots\ldots. (10)$$

$$dBX = \left(\frac{5}{8} - \mu\right)\alpha \ldots\ldots\ldots\ldots\ldots\ldots\ldots. (11)$$

$$dAXE = (2\mu - \frac{1}{2})\alpha\sqrt{2} \ldots\ldots\ldots\ldots\ldots\ldots. (12)$$

$$dBXE = (1 - 2\mu)\alpha\sqrt{2} \ldots\ldots\ldots\ldots\ldots\ldots. (13)$$

$$dBXEU = ((4\mu^2 - 3\mu + \left(\frac{11}{16}\right))^{\frac{1}{2}})\alpha \ldots.. (14)$$

Here, dAX and dBX =Bond length of tetrahedral and octahedral site
dAXE and dBXE=tetrahedral and octahedral edge
dBXEU= Unshared octahedral edge
μ=Oxygen positional parameter for LCF, the value of oxygen parameter for an ideal FCC structure=0.375 Å

The bond lengths of the tetrahedral edge (dAXE), shared-unshared octahedral edge (dBXE), and tetrahedral bond (dAX), were calculated using the lattice constant 'a' and oxygen parameter 'u', as discussed elsewhere [60], from 10, 12 and 13. Table 2 displays the calculated values, showing that as the Cd^{3+} content increases, both dAXE and dAX first decrease and then increase, along with the octahedral bond lengths dBX, by equation 12 and octahedral shared dBXE. This trend could be due to several factors, such as the larger ionic radius of Cd-Li ions compared to Fe ions, variations in the lattice constant and oxygen parameter, and the strong occupancy of Cd in the tetrahedral A site. The values for dAXE-dBXE, dAX, dBX and dBXEU (formula 14) increase from 2.9931 to 3.0192 Å, 1.8001 to 1.8158 Å, 2.0786 to 2.0967 Å and 2.9399 to 2.9656 Å with Cd^{3+} content, respectively [61]. The variation of dAX, dBX, dAXE-dBXE and dBXEU with Cd^{3+} content is concluded using Fig. 5A-C

Figure 5. A) Variation of volume of LA and LB of $Li_{1-x}Cd_xFe_2O_4$ (LCF) with x=0, 0.1, 0.2, 0.3, 0.4 B) Variation of dAx and dBx C) Variation of dAXE, dBXE and dBXEU
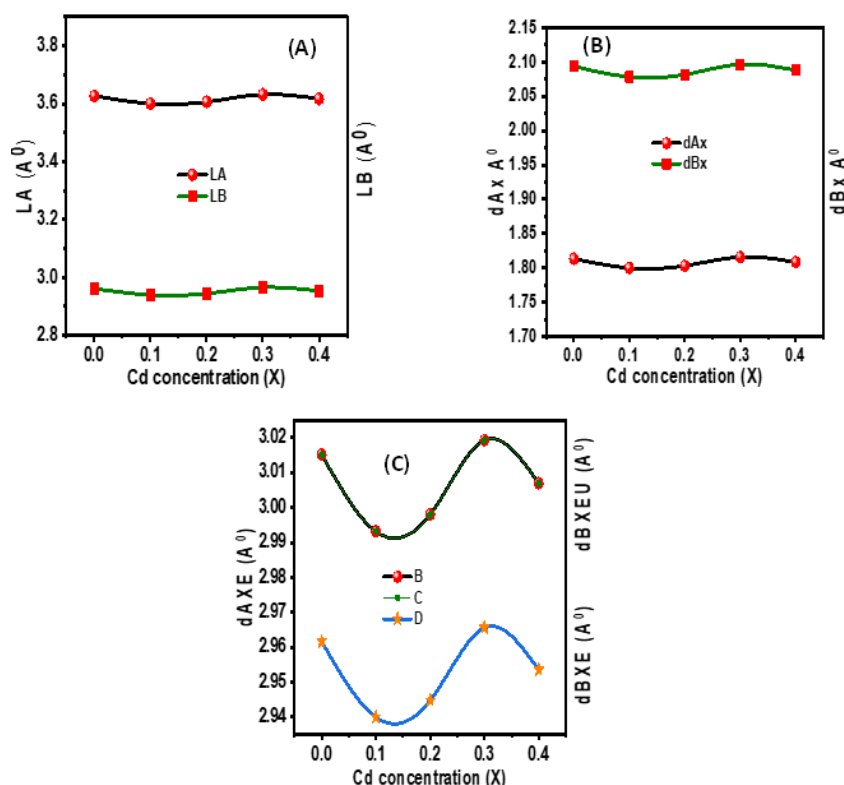

Table 2. A) Variation of LA, LB, dAx, dBx, dAXE, dBXE and dBXEU of $Li_{1-x}Cd_xFe_2O_4$ (LCF) with x=0, 0.1, 0.2, 0.3, 0.4

3.3. Fourier transform infrared spectroscopy (FTIR):

The formation of a spinel structure in ferrite samples is confirmed by analyzing the FTIR spectra of Cd^{3+} doped Lithium samples. The details of the frequency band are given in the Table 3., Fig. 6 shows the infrared spectra of all spinel, with two main broad metal-oxygen bands observed in the range of

Samples	hopping lengths (LA) (Å)	hopping lengths (LB) (Å)	dAx (Å)	dBx (Å)	dAXE (Å)	dBXE (Å)	dBXEU (Å)
LCF S1	3.6267	2.9616	1.8133	2.0939	3.0151	3.0151	2.9615
LCF S2	3.6002	2.9399	1.8001	2.0786	2.9931	2.9931	2.9399
LCF S3	3.6060	2.9447	1.8029	2.0820	2.9980	2.9980	2.9447
LCF S4	3.6316	2.9656	1.8158	2.0967	3.0192	3.0192	2.9656
LCF S5	3.6168	2.9535	1.8083	2.0882	3.0069	3.0069	2.9535

1000-300 cm^{-1}. These bands are particularly noticeable in ferrites. The higher band (v_1), usually observed in the range of 600-560 cm^{-1}, is caused by the tetrahedral metal-oxygen bond's stretching vibrations. The lowest band (v_2), usually observed in the range of 400-550 cm^{-1}, is caused by the metal-oxygen vibrations in the octahedral sites [62]. The vibrational frequencies of IR bands (v_1) and (v_2) of

samples prepared by the sol-gel auto-combustion method are given in Table 3, studied from Fig. 7A and these values match perfectly with the reported values [63]. The sample spectra show bands at 3400 and 1600 cm^{-1} which are obtained due to stretching modes and H–O–H bending vibrations of free or absorbed water. Another band near the 1400 cm^{-1} is due to antisymmetric NO-stretching vibrations caused by the nitrate group, which is present as a residue in the samples [64]. This band is very weak in the spectra of the sol-gel-derived sample, indicating the purity of Li-ferrite nanoparticles synthesized by this method. As seen from the Fig. 6, a large ionic radius of Cd^{3+} ion samples is expected to produce the v_2 shift towards lower frequencies, whereas the v_1 shift towards higher frequencies is expected with Cd^{3+} [65]. This reason can also be due to the stronger covalent bonding of Fe^{3+} ions at the tetrahedral sites than at the site of octahedral [66].

$$K_t = 4\pi^2 c^2 v_1^2 \mu \ldots \ldots \ldots \ldots \ldots \ldots \ldots (15)$$
$$K_o = 4\pi^2 c^2 v_2^2 \mu \ldots \ldots \ldots \ldots \ldots \ldots \ldots (16)$$

Where K_t and K_o are tetrahedral force constant and octahedral force constant respectively. The v_1 and v_2 are band wavenumber, where C is speed of light (2.99×10^{10} cm/s). And μ is the reduced mass for Fe^{3+} and O^{2-} ions (2.061×10^{-23} g)

The force constants (F_{tet} and F_{oct}) for the Fe^{3+}-O^{2-} band at tetrahedral and octahedral sites have been evaluated (formulae 15 and 16) and are listed in Table 3. Fig. 7B displays the variation in the force constant with Cd^{3+} for all samples at the tetrahedral and octahedral locations, F_{tet} and F_{oct} increase as Cd^{3+} rises. This is due to the fluctuation in cation-oxygen bond length. The change in bond length for the tetrahedral and octahedral sites causes the band position to shift. The radius of the impurity ion is greater than that of the displaced ion, the bond length increases. This, in turn, lowers the force constant for either site, reducing the repulsive interactions between the ions, resulting in lesser electrostatic energy and a lower wavenumber. Because Cd^{3+} has a greater ionic radius than the displaced Li^{1+} ion, a rise in forces constant is anticipated with Cd^{3+} replacement [67]. FT-IR results indicate that Li ions are stabilized in the Oh crystal field, whereas Cd^{3+} ions prefer Td-sites because of their ability to form covalent bonds [68].
The Debye temperature (θ_E) for LCF was calculated using the following equation 17, [69] to study lattice vibrations.

$$\theta_E = \frac{hcv_{av}}{K_B} \ldots \ldots \ldots \ldots \ldots \ldots \ldots \ldots \ldots \ldots \ldots \ldots (17)$$

where c is the speed of light (c = 2.99×10^{10} cm/s),
h is the Planck constant (h = 6.626×10^{-34} J·s),
K_B is the Boltzmann constant, and
v_{av} is the average wavenumber of the LCF's bands (cm^{-1}).

By examining Table 3, it is clear that the Debye temperatures (θ_E) of the samples increase from 722.5344161 to 750.4309992 K as the concentration of Cd^{3+} increases, given in Fig. 7C. This information is important in determining the conduction mechanism of these ferrites, indicates an improvement in the lattice vibrations. This suggests that the conduction in these samples is likely due to n-type electrons. The increase in θ_E can be attributed to a decrease in the wavenumber of the peak, which is typically caused by the Me-O bond vibration in the tetrahedral site [70].

Figure 6. Fourier Transform infrared spectra (FTIR) of Li$_{1-x}$Cd$_x$Fe$_2$O$_4$ (LCF) with x=0, 0.1, 0.2, 0.3, 0.4

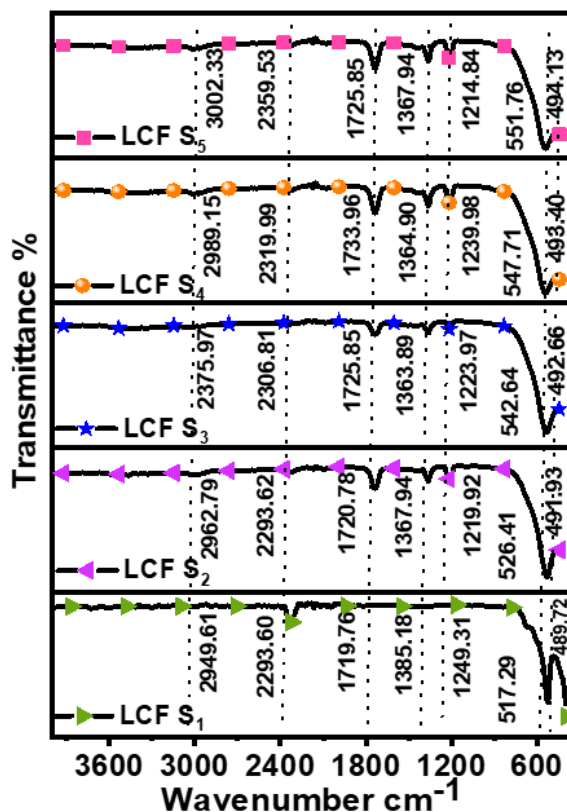**Figure 7. A) Variation of volume of octahedral metal-oxygen and tetrahedral metal oxygen of Li$_{1-x}$Cd$_x$Fe$_2$O$_4$ (LCF) with x=0, 0.1, 0.2, 0.3, 0.4 B) Variation of force constant for octahedral and tetrahedral site C) Variation of Debye temperature**
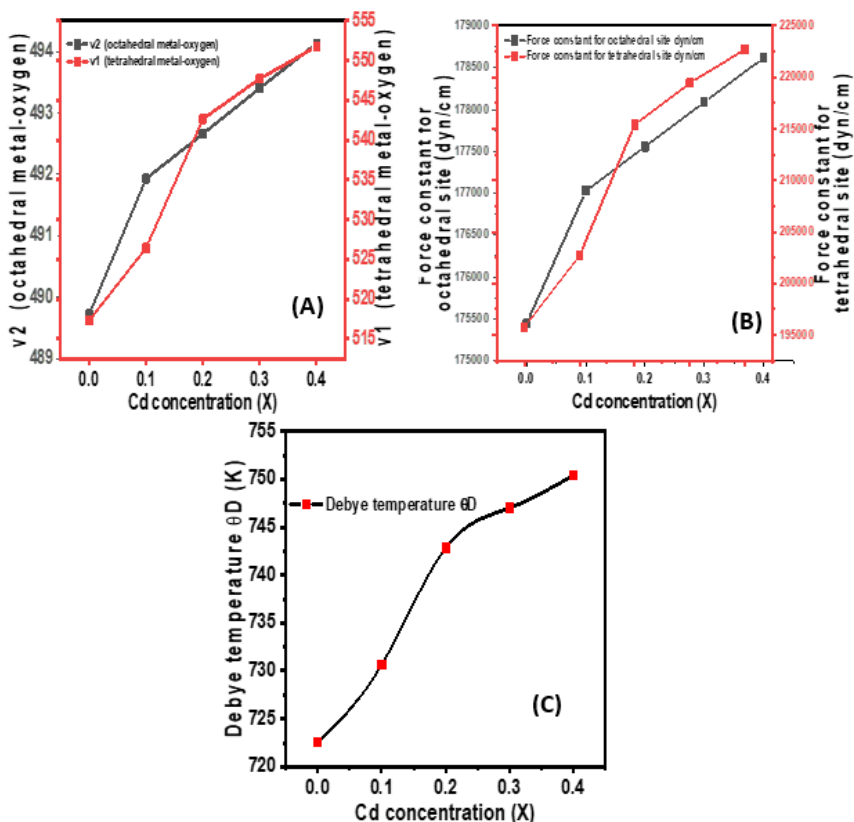
Table 3. List of v_2, v_1, force constant for octahedral, force constant tetrahedral and Debye temperature by FTIR spectra of $Li_{1-x}Cd_xFe_2O_4$ (LCF) with x=0, 0.1, 0.2, 0.3, 0.4

Samples	v_2 (octahedral metal-oxygen) cm^{-1}	v_1 (tetrahedral metal-oxygen) cm^{-1}	force constant for octahedral (dyne/cm)	force constant tetrahedral (dyne/cm)	Debye temperature (K)
LCF S_1	489.72	517.29	175442.2716	195752.7873	722.5344161
LCF S_2	491.93	526.41	177029.7196	202716.0104	730.6637444
LCF S_3	492.66	542.64	177555.608	215408.7779	742.8326243
LCF S_4	493.40	547.71	178089.4034	219452.8014	747.0013266
LCF S_5	494.13	551.76	178616.7704	222710.2547	750.4309992

Table 4. List of Frequency band, group and appearance in FTIR spectra of $Li_{1-x}Cd_xFe_2O_4$ (LCF) with x=0, 0.1, 0.2, 0.3, 0.4

Frequency Range	Wavenumber cm^{-1}	Group	Appearance
400 to 4000 cm^{-1}	400-500	v_2 (octahedral metal-oxygen)	Strong
	560-600	v_1 (tetrahedral metal-oxygen)	Strong
	1000-1280	Aliphatic C-O	Strong
	1300-1400	Nitrogen	Strong
	1600	H-O-H bending (free or absorbed water)	Medium
	2300	O=C=O (carbon dioxide)	Weak
	3000-3400	N-H stretching	Medium

3.4. Vibrating Sample Microscope (VSM):

Fig. 8A portrays the hysteresis plot of all the samples of LCF, and Table 5 outlines the impact of Cd doping on saturation magnetization (M_s), coercivity (H_c), and remanence (M_r). The magnetic behavior of LCF can be well explained by Neel's two sublattice models [72]. According to this model, a spinel having an AB_2O_4 structure has two types of sublattices, i.e., A and B sites. Due to exchange energy, the ions occupying A and B sites have their magnetic moments arranged antiparallelly. In this case, Fe^{3+} ions are evenly distributed amongst the A and B sites, whereas Li^{1+} ions prefer B sites more strongly. The net magnetic moment is determined by Li^{1+} ($\mu B=2$) ions as, due to Fe^{3+} ($\mu B=5$) ions

present at both sites, the same cancel out [73]. Therefore, the overall magnetization of the material is the difference in magnetization present at these two sites, with the B site dominating due to it containing more ions. When Cd^{3+} is replaced with nonmagnetic Li^{1+} ions, the magnetic behavior of the material shows an interesting trend. The magnetization (Ms) initially increases up to x=0.2, then decreases up to x=0.3, and finally proceeds to increase up to x=0.4. This behavior can be explained based on the exchange interactions such as A-B, A-A, and B-B, which depend on the distribution of magnetic and non-magnetic ions in the spinel network at A and B-sites [74]. Moreover, Cd^{3+} has a strong preference for A sites, which leads to the dislocation of some Fe^{3+} ions from A to B sites. In contrast to LCF, the compensation in the magnetic moment of Fe^{3+} does not occur, and they contribute with large magnetic moments to B sites, increasing magnetization. It is interesting to note that after x=0.3 concentration, the A-B exchange interaction is weakened due to the altering of the parallel orientation of the magnetic moments at the B sites, which compensate for each other only partially. Although the minimum value of coercivity (H_c) is obtained for x=0.2, there is a general fluctuation trend for increasing Cd^{3+}. This fluctuation might be attributed to the alternation of particle and grain size of Li ferrite before and after Cd doping. The Fig. 8B illustrates the fluctuation of M_s and H_c with Cd^{3+} content, providing an important insight into the magnetic behavior of the material [75].

In LCF, magneto-crystalline anisotropy is estimated using this formula 18 [76].

$$H_c = \frac{2K}{M_s} \ldots \ldots \ldots \ldots \ldots \ldots \ldots \ldots \ldots \ldots \ldots \ldots \ldots \ldots (18)$$

The data presented in Table 5 highlights an interesting observation, where an increase in Cd^{3+} concentration leads to an increase in the anisotropy (K) value. This increase in K is attributed to the corresponding increase in the coercive force, which exhibits significant variation with an increase in Cd^{3+} concentration. This finding suggests that a higher concentration of Cd^{3+} tends to occupy *B*-sites, leading to a noticeable rise in the K value. Importantly, the K value shows a significant increase from 133898.477 to 337380.907 erg/cm^3 with an increase in the Cd^{3+} amount. This observation could have potential implications in the design and development of new materials with improved magnetic properties.

$$n_\beta = \frac{M_s * Molecular\ Wt}{5585} \ldots \ldots \ldots \ldots \ldots \ldots \ldots \ldots \ldots \ldots \ldots \ldots . (19)$$

To calculate the number of Bohr magnetons per formula unit, we consider the saturation magnetization and molecular weight of each composition using the equation 19 [77], given in the Table. It is worth noting that the trends in the variation of the number of Bohr magnetons per formula unit derived from the proposed cation distribution and that from the saturation magnetization measurements show a good agreement. The non-linear variation of μ_B highlights the possibility of spin canting as the mechanism controlling magnetization in the LCF [78]. The Cd^{3+} substitution in Li ferrite results in a triangular arrangement of spins at the octahedral sites of the LCF. In the present LCF, it is observed that the values of μ_B increased from 1.54598 to 2.44153 with Cd^{3+} content. This indicates that spin canting is effective for x=0.2, where the angle of spin canting continuously increases with Cd. As a result, the value of μ_B decreases from 2.2958 to 2.01372. This information is important as it provides insight into the factors affecting the magnetization in LCF and highlights the potential for spin canting as a mechanism to control magnetization in similar materials.

$$Remanence\ ratio = \frac{Mr}{Ms} \ldots \ldots \ldots \ldots \ldots \ldots \ldots \ldots \ldots \ldots \ldots \ldots \ldots . . (20)$$

The remanence of a LCF plays a crucial role in determining its potential as a magnetic recording medium [79]. The remanence ratio, also known as the squareness, provides useful information about the ease with which the magnetic axis aligns itself with the nearest direction after the external magnetic field is removed, calculated using formula 20. In LCF, observed a varying range of remanence ratio, which was from 0.3136810 to 0.402965. Ratios less than 0.5 suggest an isotropic nature of the LCF,

which could be further studied to enhance their magnetic properties. The variation of μB and remanence ratio with Cd^{3+} ions is shown in the Fig. 8C.

Figure 8. A) Vibration sample magnetometer (VSM) Li$_{1-x}$Cd$_x$Fe$_2$O$_4$ (LCF) with x=0, 0.1, 0.2, 0.3, 0.4 B) Variation of saturation magnetization and coercivity C) Variation of Bohr magneton and magnetization ratio
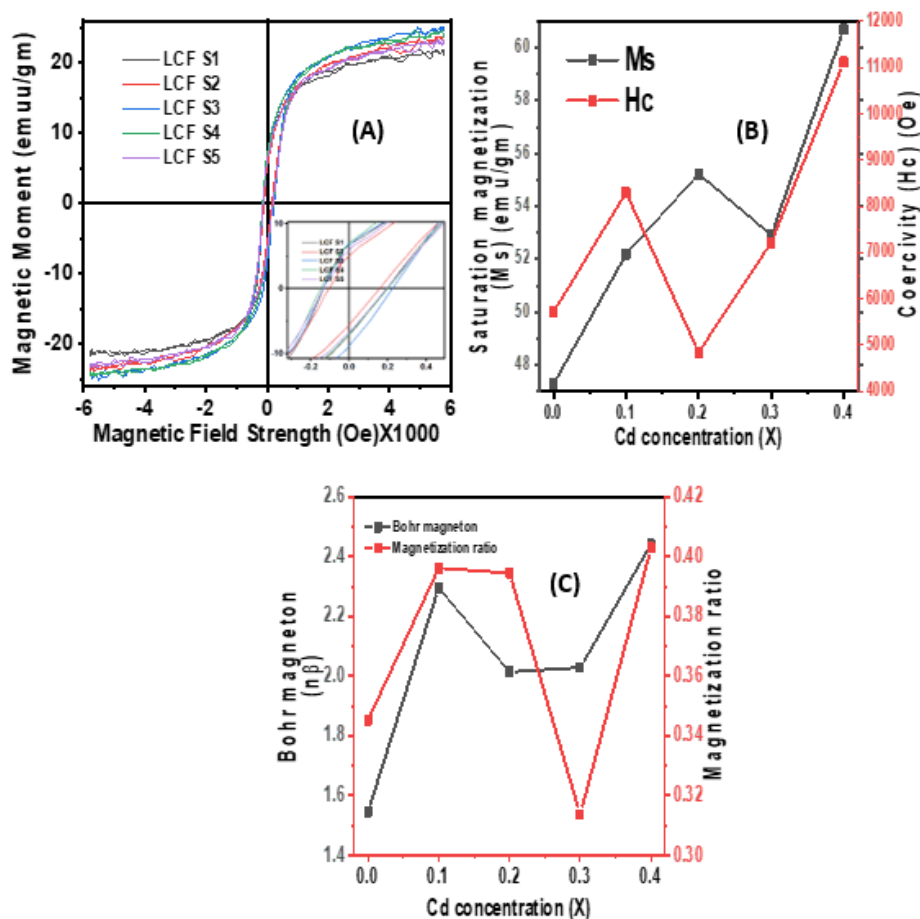

Table 5. List of Ms, Mr, Hc, K, nB and Mr/Ms of Li$_{1-x}$Cd$_x$Fe$_2$O$_4$ (LCF) with x=0, 0.1, 0.2, 0.3, 0.4

Samples	Ms (emu/gm)	Mr (emu/gm)	Hc (Oe)	Anisotropy constant (K) (erg/cm³)	Molecular weight (g/mol)	Bohr magneton (μB)	Remanence ratio (Mr/Ms)
LCF S₁	47.2800	16.3200	5714.0759	135080.754	182.621	1.54598404	0.345177665
LCF S₂	52.2000	20.6800	8302.6205	216698.395	245.635	2.29582049	0.396168582
LCF S₃	55.2300	21.7900	4848.7589	133898.477	203.633	2.01372239	0.394531957
LCF S₄	52.9200	16.6000	7221.7191	191086.687	214.139	2.02904566	0.313681028
LCF S₅	60.7000	24.4600	11116.339	337380.907	224.645	2.44152681	0.402965404

3.5. UV-visible absorption study:

In the 400–800 nm range, LCF with x = 0 to 0.4 displays interesting absorption spectra as seen in Fig. 9A. We calculated the band gap energy value (Eg) by plotting $[\alpha h\nu]^2$ against the photon energy $[h\nu]$ [80] as shown in Fig. 9B, which varies from 2.17 to 3.39 eV.

The optical band gap energy (E_g) was calculated by the following Tauc relation 21 [81]:

$$(\alpha h\nu)^{1/n} = (h\nu - Eg)A \ldots\ldots\ldots\ldots\ldots\ldots (21)$$

where α = absorption coefficient,

Eg = the gap energy,

hν = the energy of the incident radiation expressed in (eV),

A is a constant, and

n = the exponent characterizes the type of optical transition.

Our ferrite sample shows semiconducting activity based on the band gap energy value, given in Table 6, which makes it a promising candidate for various technical domains such as optoelectronics, photovoltaics, and gas sensors. During the formation of LCF, Li^{1+} fits in Cd^{3+}. Impurity bands are created due to the formation of the level of impurity inside an energy gap. The distance between the valence band and the lowest impurity band acts like an effective band gap [82]. At a high concentration of dopant Cd^{3+}, the distance between impurity bands increases. The bands could overlap together, leading to a decrease in band gap energy. The calculated band gap values given in Table 6. Overall, these findings are promising for the development of new materials with potential applications in various technical domains.

Figure 9. A) UV-visible absorption spectra of $Li_{1-x}Cd_xFe_2O_4$ (LCF) with x=0, 0.1, 0.2, 0.3, 0.4 B) Tauc plot
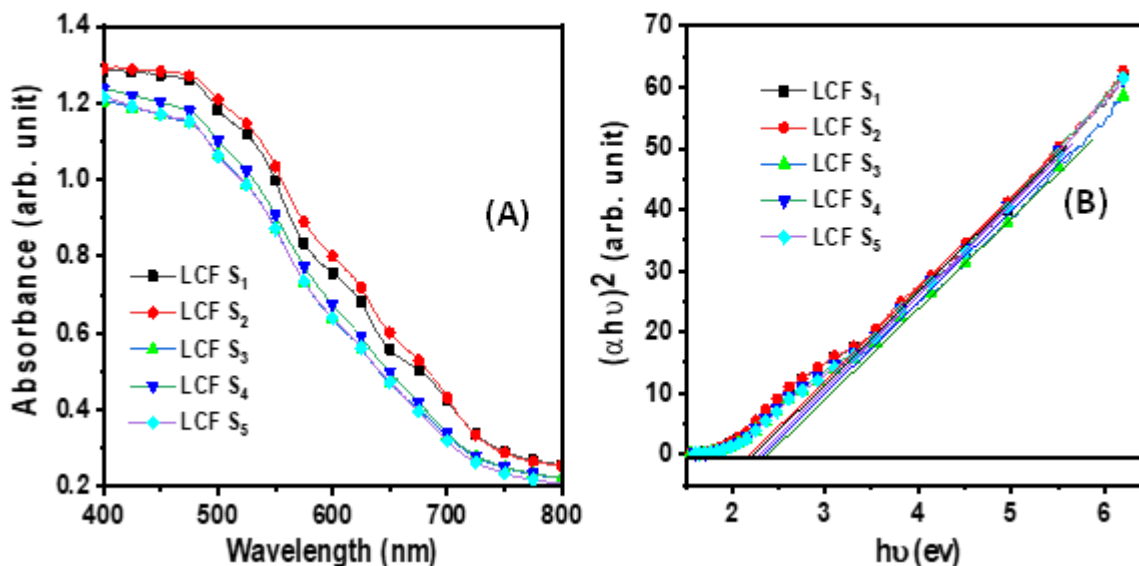
Table 6. Variation of band gap of $Li_{1-x}Cd_xFe_2O_4$ (LCF) with x=0, 0.1, 0.2, 0.3, 0.4

Samples	Band gap (ev)
LCF S_1	2.22
LCF S_2	2.17
LCF S_3	2.34
LCF S_4	3.39
LCF S_5	2.29

3.6. Field emission scanning electron microscopy (FE-SEM):

The FESEM images of LCF S_2 nanoparticles (x= 0.1) in Fig. 10 A and C. It's interesting to note that the average grain size obtained from FESEM images is larger than the crystallite size determined by XRD measurement, indicating the presence of agglomeration in the nanoparticles [83]. However, the LCF S_2 nanoparticles have a uniform and spherical shape. Although the particles are irregular and agglomerated, the sol-gel auto-combustion method produced LCF nanoparticles with a uniform, mono-disperse, and spherical and cubic structure with a narrow particle size distribution. The histogram of the LCF S_2 is shown in Fig. 10 B and D.

Figure 10. A) Field emission scanning electron microscopy (FE-SEM) of $Li_{1-x}Cd_xFe_2O_4$ (LCF S_2) at x=0.1 (scale 500 nm), B) Histogram of LCF S_2 C) FE-SEM image of LCF S_2 (scale 2 μm) D) Histogram of LCF S_2
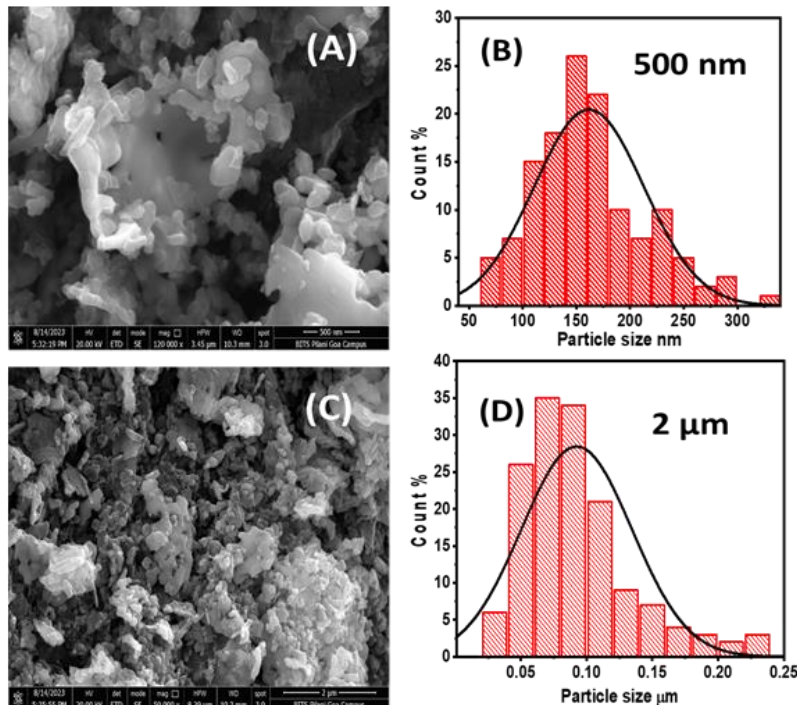
3.7. The Williamson-Hall analysis (W-H plot):

The analysis of the size and strain broadening of a Bragg peak is a crucial step in understanding the properties of crystalline LCF. In this regard, the Williamson-Hall (W-H) method has played a pivotal role in separating these two effects by analyzing their distinct angle (θ) dependencies [84]. By plotting βcos θ against sin θ, as shown in Fig. 11 A, the W-H analysis provides better information on the strain (ε) induced in the crystal lattice and the size of the crystallites in the LCF. The resulting linear equation

(y=mx+c, where m = strain and c = 1/D) allows for the determination of lattice strain (ε) from the slope and the crystallite size (D) from the intercept, using relation 22. To determine D and ε using the W-H method, the modified Scherer relation was used [84]. Overall, the W-H analysis method has proven to be a reliable and effective way of analyzing the size and strain broadening of Bragg peaks, which is essential for understanding the properties of crystalline materials [85]. The observed noticeable change in strain is detailed in Fig. 11 B.

$$\beta cos\theta = \frac{0.9\lambda}{D} + 4\varepsilon sin\theta \ldots\ldots\ldots\ldots\ldots\ldots\ldots\ldots\ldots\ldots(22)$$

The addition of Cd^{3+} ions has resulted in a significant decrease in crystallite size from 32 to 11 nm. The calculated crystallite sizes from W-H plots (Table 7) are in line with those calculated by Scherer's formula, indicating a high level of accuracy. It's interesting to note that the lattice strain is of tensile type and varies from 0.0007975 to 0.00378, with a minimum value of 0.002611 at x=0.4. This variation in lattice strain corresponds to the variation in 'a', which demonstrates the effect of larger Cd^{3+} ion substitution for smaller Fe^{3+} ions, given in Fig. 11 B [86].

Figure 11. A) The Williamson-Hall plot of $Li_{1-x}Cd_xFe_2O_4$ (LCF) with x=0, 0.1, 0.2, 0.3, 0.4 B) variation of crystallite size and strain
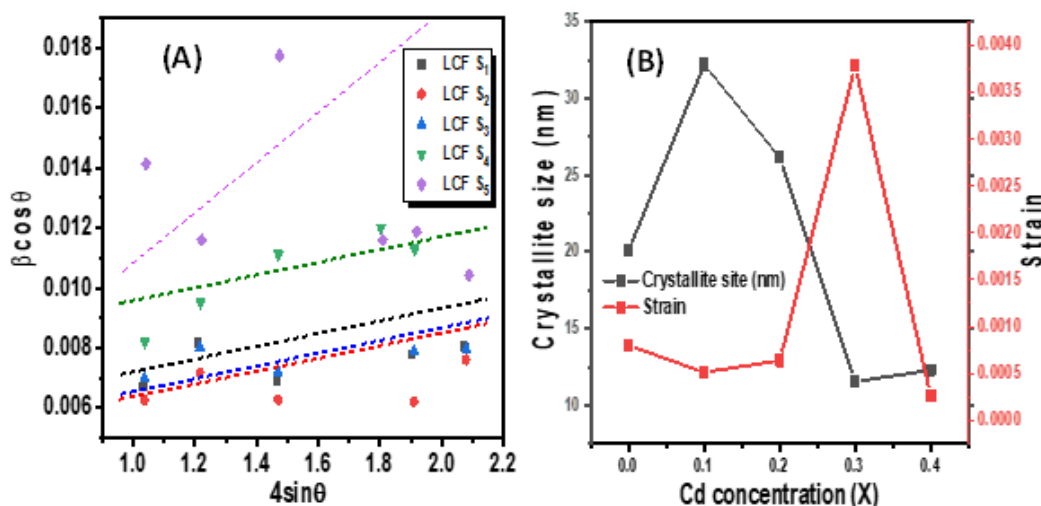

Table 7. Variation of crystallite size and strain of $Li_{1-x}Cd_xFe_2O_4$ (LCF) with x=0, 0.1, 0.2, 0.3, 0.4

| Samples	Equation Y=mx+c	Crystallite size (D) (nm)	Strain (m=ε)
LCF S_1	0.000796x+0.0069	20.09	0.0007975
LCF S_2	0.000511x+0.0043	32.23	0.0005115
LCF S_3	0.000636x+0.0053	26.15	0.0006362
LCF S_4	0.00378x+0.012	11.55	0.00378
LCF S_5	0.000261x+0.01127	12.30	0.0002611

3.8. Dielectric constant:

Fig. 12 shows the change in the dielectric constant with the log of frequency of LCF at x=0, 0.2 and 0.4. This study aimed to investigate the change in the dielectric constant of Lithium Ferrite (LCF) with the frequency at different concentrations of Cadmium (Cd^{3+}). The results showed that the dielectric constant decreases sharply at low frequencies and gradually decreases as the frequency increases. The addition of Cd^{3+} to LCF increased the dielectric constant, reaching its maximum value at x=0.4 [87]

Understanding the mechanism of polarization is key to interpreting the behavior of the dielectric constant. The four types of polarization - electronic polarization, ionic polarization, orientation polarization, and interfacial polarization - were considered in this study, as the frequency range used covered all four types [88]. The high dielectric constant values observed in this study are mainly due to interfacial polarization, which is generated by a localized accumulation of charges at the points of crystal defects or spaces. This results in the emergence of dipolar materials [89]. Interfacial polarization requires a low frequency and stops quickly, leading to a relaxation time that is almost zero. The increase in the dielectric constant of LCF when Cd^{3+} is added can be explained by its optical properties, which have a large reflection factor. The increase in the dielectric constant is directly related to the reflection factor. These findings can provide a better understanding of the behavior of dielectric constants in general and can have potential applications in various fields. The dielectric constant is increased proportionally to the reflection factor i.e. equation 23 [90].

$$\varepsilon = (n + iK)^2 \dots\dots\dots\dots\dots\dots\dots\dots\dots\dots\dots\dots. (23)$$

where ε is the dielectric constant,

n is the reflection factor,

K is the extinction coefficient.

Figure 12. Dielectric constant with log f of $Li_{1-x}Cd_xFe_2O_4$ (LCF) with x=0, 0.1, 0.2, 0.3, 0.4
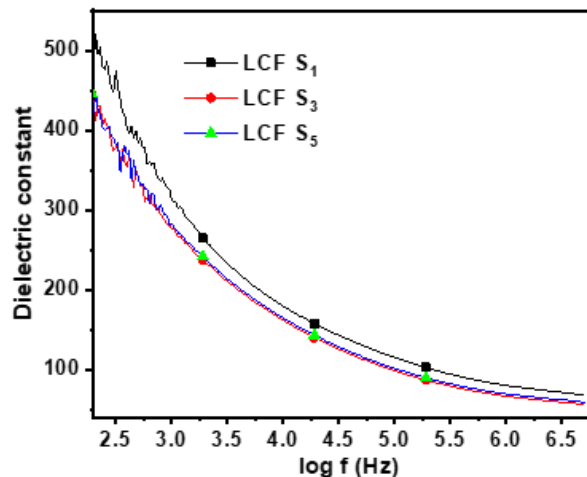
3.9. Conductivity:

$$\varepsilon = \frac{\sigma}{i\varepsilon_0\acute{\omega}} \dots\dots\dots\dots\dots\dots\dots\dots\dots\dots\dots\dots\dots\dots (24)$$

where ε is the dielectric constant,

ε_0 is permissibility, and

ω is the angular frequency of the applied current.

The conductivity of a material is directly proportional to its frequency and can be observed through the following equation 24. As per Equation (4), the conductivity values are determined by the imaginary dielectric constant and the frequency, while other values remain constant. In comparison to the frequency, the dielectric constant values are relatively small. Therefore, frequency plays a crucial role in determining the increase in conductivity, which is also indicative of the loss of power and the subsequent generation of heat due to the spinning of the dipolar or the vibration of charges with the change in range. Consequently, the study of conductivity depends significantly on frequency [91]. In addition, Fig. 13 demonstrates that the conductivity increases with Cd^{3+} content. This increase in conductivity can be attributed to the rise in density, which is linked to the energy band gap of LCF.

Figure 13. Conductivity with log f of $Li_{1-x}Cd_xFe_2O_4$ (LCF) with x=0, 0.1, 0.2, 0.3, 0.4
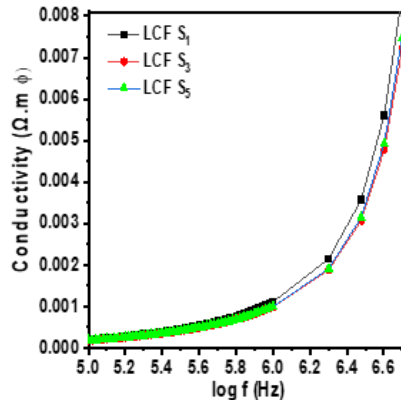
3.10. Transmission Electron Microscopy (TEM):

In Fig. 14 A-B of TEM, we observed the LCF S_2 nanoparticles (x= 0.1) synthesized using the sol-gel auto-combustion technique. These particles appear to be well dispersed with high crystalline structures and uniform size distributions, forming approximately spherical shapes with an average size distribution of 38.96 nm. It is worth noting that these particles exhibit super-ferromagnetic nature, which is a significant observation. Furthermore, Fig. 14 C shows the patterns of selective area electron diffraction (SAED) of the samples. These patterns reveal the polycrystalline nature of LCF S_2 with high crystallinity. The bright spot obtained with the Debye ring pattern represents the polycrystalline nature of the sample. These observations provide valuable insights into the properties of LCF S_2 nanoparticles synthesized using the sol-gel auto-combustion technique [92]. The Fig. 14 D represents a histogram of the particle size in vertical bars of LCF S_2, obtained from the TEM micrographs. The parameters of the LCF S_2 size distribution were obtained from the standard approach. The solid line in the histogram is curve fitting using the function of log-normal.

Figure 14. A) Transmission Electron Microscopy (TEM) of $Li_{1-x}Cd_xFe_2O_4$ (LCF S_2) (scale 200 nm), B) TEM (scale 50 nm) C) SAED pattern D) Histogram of image scale 200 nm
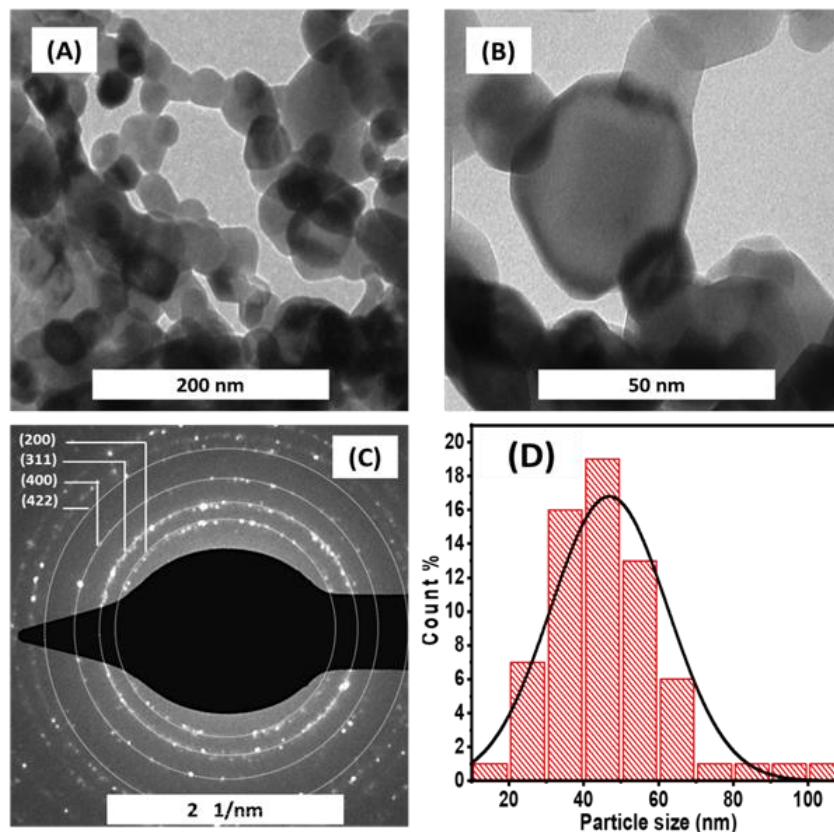
4. Conclusion:

Systematic work was carried out in the successful preparation of cadmium-doped Lithium ferrite (LCF) nanoparticles through the sol-gel auto-combustion method, having chemical compositions of $Li_{1-x}Cd_xFe_2O_4$ at x=0, 0.1, 0.2, 0.3, 0.4. The X-ray diffraction (XRD) data showed a single cubic phase, while the selected area electron diffraction (SAED) profile confirmed the creation of single-phase spinel LCF. The estimated crystallite sizes were consistent with the calculated sizes from XRD data, which was confirmed by the particle sizes obtained from Field emission scanning electron microscopy (FE-SEM) and transmission electron microscopy (TEM). As Cd^{3+} ion concentration increased, there was a non-linear variation in lattice parameters, and this may be due to the structural imperfections created by the substitution of Cd^{3+} ions for Fe^{3+} ions. The Fourier transform infrared (FTIR) spectra of the LCF confirmed the formation of Spinel ferrite, while the variation in magnetic properties due to Cd^{3+} ions' substitution suggested the creation of a frustrated magnetic structure within the LCF. The saturation magnetization, coercivity, and remanence were influenced by both the particle size and Cd^{3+} composition. The remanence ratio values suggested the isotropic behavior of the LCF. Overall, the results show that the prepared LCF nanoparticles are a promising material with potential applications in magnetic and electronic devices. The observed lattice constant of LCF and the non-linear variation of lattice parameters provide insight into the structural imperfections created by the substituted Cd^{3+} ions. The variation in magnetic properties and dielectric constant values also provide useful information for further research and development. The LCF nanoparticles prepared with x=0.2 show promising potential for various energy storage applications in magnetic and electronic devices like, Sensors, batteries, supercapacitors, etc.

References:

1. Samer Bayda, Muhammad Adeel, Tiziano Tuccinardi, Marco Cordani, and Flavio Rizzolio (2020), "The History of Nanoscience and Nanotechnology : From Chemical–Physical Applications to Nanomedicine", Molecules, Vol. 25, 112

2. Dan Guo, Guoxin Xie and Jianbin Luo (2014), "Mechanical properties of nanoparticles: basics and applications", J. Phys. D: Appl. Phys., Vol. 47, 013001

3. Shameran Jamal Salih and Wali M. Mahmood (2023), "Review on magnetic spinel ferrite (MFe_2O_4) nanoparticles: From synthesis to application", Heliyon, Vol. 9, e16601

4. S. A. Mazen, H. M. Elsayed, N. I. Abu-Elsaad (2020), "Effect of divalent metal ions substitution on structural and magnetic properties of $Li_{0.25}Mn_{0.5-x}M_xFe_{2.25}O_4$ (M = Co^{2+}, Ni^{2+}, Cu^{2+}) spinel ferrites", Materials Chemistry and Physics, Vol. 256, 123676

5. Sagar Kumar Dutta, Morsheda Akhter, Jamil Ahmed, Md. Khairul Amin, Palash Kumar Dhar (2022), "Synthesis and Catalytic Activity of Spinel Ferrites: A Brief Review", Biointerface Research in Applied Chemistry, Vol. 12, 4, pp4399 – 4416

6. Bindiya Dey, M. Bououdina, G. Abd elfadeel, P. Dhamodharan, S. Asath Bahadur, M. Venkateshwarlu and C. Manoharan (2023), "Tuning the gas sensing properties of spinel ferrite NiFe2O4 nanoparticles by Cu doping", Journal of Alloys and Compounds, Vol. 172711

7. Sagar Mitra, Pavan S. Veluri, Antara Chakraborthy, and Ramesh K. Petla (2014), "Electrochemical Properties of Spinel Cobalt Ferrite Nanoparticles with Sodium Alginate as Interactive Binder", ChemElectroChem, Vol. 1, pp1068-1074

8. Al-Najar B, Kamel AH, Albuflasa H and Hankins NP (2023), "Spinel ferrite nanoparticles as potential materials in chlorophenol removal from wastewater", Environ Sci Pollut Res Int Vol. 30, 48, pp104976-104997

9. Ebtesam E. Ateia, Mahmoud A. Ateia, Motaz G. Fayed, Soliman. I. El-Hout, Saad G. Mohamed and M. M. Arman (2022), "Synthesis of nanocubic lithium cobalt ferrite toward high-performance lithium-ion battery", Applied Physics A, Vol. 128, 483

10. H. Kennaz, A. Harat, O. Guellati, D. Y. Momodu, F. Barzegar, J. K. Dangbegnon, N. Manyala and M. Guerioune (2018), "Synthesis and electrochemical investigation of spinel cobalt ferrite

magnetic nanoparticles for supercapacitor application", J Solid State Electrochem, Vol. 22, pp835–847

11. Ajitanshu Vedrtnam, Kishor Kalauni, Sunil Dubey and Aman Kumar (2023), "A comprehensive study on structure, properties, synthesis and characterization of ferrites", AIMS Materials Science, Vol. 7, 6, pp800–835

12. S. D. Sartale, Chandrakant Lokhande and M. Muller (2003), "Electrochemical synthesis of nanocrystalline $CuFe_2O_4$ thin films from non-aqueous (ethylene glycol) medium", Materials Chemistry and Physics, Vol. 80, pp120-128

13. Rutuja Prashant Gambhir, Sonali S Rohiwal and Arpita Pandey Tiwari (2022), "Multifunctional surface functionalized magnetic iron oxide nanoparticles for biomedical applications: A review", Applied Surface Science Advances, Vol. 11, 100303

14. Oscar Oehlsen, Sussy I. Cervantes-Ramirez, Pabel Cervantes-Aviles and Illya A. Medina-Velo (2022), "Approaches on Ferrofluid Synthesis and Applications: Current Status and Future Perspectives", ACS Omega, Vol. 7, 4, pp3134-3150

15. Amyn S. Teja and Pei-Yoong Koh (2009), "Synthesis, properties, and applications of magnetic iron oxide nanoparticles", Progress in Crystal Growth and Characterization of Materials, Vol. 55, 22-45

16. Mona Ebadi, Kalaivani Buskaran, Saifullah Bullo, Mohd Zobir Hussein, Sharida Fakurazi and Giorgia Pastorin (2021), "Drug delivery system based on magnetic iron oxide nanoparticles coated with (polyvinyl alcohol-zinc/aluminium-layered double hydroxide-sorafenib)", Alexandria Engineering Journal Vol. 60, pp733-747

17. Samuel D. Oberdick, Stephen E. Russek, Megan E. Poormana and Gary Zabow (2012), "Observation of iron oxide nanoparticle synthesis in magnetogels using magnetic resonance imaging", Soft Matter Vol. 00, pp1-3

18. Shaimaa Helayl, Salah Hassab-Elnaby, Yehia Badr and Abeer Salah (2023), "Nonlinear optical absorption and optical limiting of magnetic iron oxide nanomaterials", SN Applied Sciences Vol. 5, 229

19. Atta Ur Rehman, N. A. Morley, Nasir Amina, Muhammad Imran Arshad, Muhammad Ajaz, Nabia, Khalid Mahmood, Adnan Alia, Asma Aslam, Aisha Bibi, Muhammad Zahir Iqbal, Faisal Iqbal, N. Bano and Meshal Alzaid (2022), "Controllable Synthesis of La^{3+} doped $Zn_{0.5}Co_{0.25}Cu_{0.25}Fe_{2-x}La_xO_4$ (x = 0.0, 0.0125, 0.025, 0.0375, 0.05) nano-ferrites by Sol-Gel Auto-Combustion Route", Ceramics International, Vol. 46, 18, pp29297-29308

20. Hang Xu, Chuanqiang Yin, Xinran Hou, Man Gong, Changshu Yang, Lexiang Xu, Jinpeng Luo, Lei Ma, Lang Zhou and Xiaomin Li (2022), "Polyimide-derived carbon nanofiber membranes as free-standing anodes for lithium-ion batteries", RSC Adv, Vol. 12, 21904

21. Mukhtar Ahmad, Muhammad Shahid, Yousef Mohammed Alanazi, Atiq Rehman, Muahmmad Asif, Charles W. Dunnill (2022), "Lithium ferrite (Li0.5Fe2.5O4): synthesis, structural, morphological and magnetic evaluation for storage devices", Journal of Materials Research and Technology, Vol.18, pp3386-3395

22. S. S Bellad, S. C Watawe and B. K Chougule (1999), "Microstructure and permeability studies of mixed Li-Cd ferrites", Journal of Magnetism and Magnetic Materials Vol. 195, 1, pp57-64

23. M. A. Almessiere, Y. Slimani, Demir Korkmaz, A. Baykal, H. Gunguneş, H. Sozeri, Sagar E. Shirsath, S. Güner, S. Akhtar, and A. Manikandan (2019), "Impact of La^{3+} and Y^{3+} ion substitutions on structural, magnetic and microwave properties of $Ni_{0.3}Cu_{0.3}Zn_{0.4}Fe_2O_4$ nanospinel ferrites synthesized via sonochemical route", RSC Adv., Vol. 9, 53, pp30671-30684

24. Bo Niu, Fan Zhang, Hang Ping, Na Li, Jieyang Zhou, Liwen Lei, Jingjing Xie, Jinyong Zhang, Weimin Wang and Zhengyi Fu (2017), "Sol-gel Autocombustion Synthesis of Nanocrystalline High-entropy Alloys", Sci Rep. Vol. 7, 3421

25. M. Niederberger and N. Pinna (2009), "Metal Oxide Nanoparticles in Organic Solvents: Synthesis, Formation, Assembly and Application (Engineering Materials and Processes)", Springer, Berlin, Germnay

26. A. Feinle, M. S. Elsaesser, and N. Husing (2016), "Sol-gel synthesis of monolithic materials with hierarchical porosity", Chemical Society Reviews, Vol. 45, pp3377–3399

27. M. Haruta (2004), "Nanoparticulate gold catalysts for low-temperature CO oxidation", Journal of New Materials for Electrochemical Systems, Vol. 7, pp163–172

28. R. Xu, D. Wang, J. Zhang, and Y. Li (2006), "Shape-dependent catalytic activity of silver nanoparticles for the oxidation of styrene", Chemistry - An Asian Journal, Vol. 1, 6, pp888–893

29. I. A. Rahman and V. Padavettan (2012), "Synthesis of silica nanoparticles by sol-gel: size-dependent properties, surface modification, and applications in silica-polymer nanocomposites—a review", Journal of Nanomaterials, Vol. 132424, pp1-15

30. R. Ullah and J. Dutta (2008), "Photocatalytic degradation of organic dyes with manganese-doped ZnO nanoparticles", Journal of Hazardous Materials Vol. 156, pp194–200

31. R. Verma, B. Mantri, and A. K. Srivastava (2015), "Shape control synthesis, characterizations, mechanisms and optical properties of large scaled metal oxide nanostructures of ZnO and TiO2", Advanced Materials Letters Vol. 6, 4, pp324–333

32. B. G. Toksha, S. E. Shirsath, S. M. Patange and K. M. Jadhav (2008), "Structural investigations and magnetic properties of cobalt ferrite nanoparticles prepared by sol–gel auto combustion method", Solid State Commun, Vol. 147, pp479–483

33. A. K. Zak, M. E. Abrishami, W. A. Majid, R. Yousefi and S. M. Hosseini (2011), "Effects of annealing temperature on some structural and optical properties of ZnO nanoparticles prepared by a modified sol–gel combustion method", Ceram. Int., Vol. 37, 1, pp393–398

34. R. P. Sharma, S. D. Raut, R. M. Mulani (2019), "Sol–gel auto-combustion mediated cobalt ferrite nanoparticles: a potential material for antimicrobial applications", Int Nano Lett, Vol. 9, pp141–147

35. Tsering Namgyal, Jagdish Singh, Kailash Chandra, S. Bansal and Sonal Singhal, δ-Phase evolution in Cd-doped lithium ferrites: Their thermal, electrical and magnetic properties, Journal of Molecular Structure, Vol. 1019, pp 103-109

36. Hu Yang, Xingxing Yang, Jinpei Lin, Fang Yang, Yun He and Qing Lin (2023), "Effect of Cd2+ Substitution on Structural-Magnetic and Dielectric Properties of Ni-Cu-Zn Spinel Ferrite Nanomaterials by Sol-Gel", Molecules, Vol. 17, 6110

37. S. Malathi, B. Sridhar and Shiferaw Garoma Wayessa (2023), "A Study of Lithium Ferrite and Vanadium-Doped Lithium Ferrite Nanoparticles Based on the Structural, Optical, and Magnetic Properties", Journal of Nanomaterials, Vol. 6752950, pp1-7

38. P. Hajasharif, K. Ramesh, S. Sivakumar, P. Sivagurunathan (2019), "Synthesis and Characterization of Copper Doped Lithium Ferrite Nanocomposite", International Journal of Innovative Technology and Exploring Engineering (IJITEE), Vol. 9, 2

39. Vivek Verma, Prachi Sharma And Adarsh Singh (2014), "Effect of iron content on permeability and power loss characteristics of $Li_{0.35}Cd_{0.3}Fe_{2.35}O_4$ and $Li_{0.35}Zn_{0.3}Fe_{2.35}O_4$", Bull. Mater. Sci., Vol. 37, 4, pp855-859

40. Na Wu, Xue Zhang, Can Ma, Ya-Ru Shi, Jin-Ming Zhou, Zhe Wang, Hui Liu, Xian-Xiang Zeng and Yu Wei (2019), "High performance isomeric Fe_2O_3 nanospheres anode materials derived from industrial wastewater for lithium ion batteries", Electrochimica Acta, Vol. 297, pp1028-1034

41. Simi Debnath, Krishna Deb, Biswajit Saha and Ratan Das (2019), "X-ray diffraction analysis for the determination of elastic properties of zinc-doped manganese spinel ferrite nanocrystals ($Mn_{0.75}Zn_{0.25}Fe_2O_4$), along with the determination of ionic radii, bond lengths, and hopping lengths", Journal of Physics and Chemistry of Solids, Vol. 134, pp105-114

42. S. Akhter, M.A. Hakim (2010), "Magnetic properties of cadmium substituted lithium ferrites", Materials Chemistry and Physics, Vol. 120, pp399-403

43. JCPD card no: 40-1117

44. A. R. Chavan, S. B. Somvanshi, P. P. Khirade and K. M. Jadhav (2020), "Influence of trivalent Cr ion substitution on the physicochemical, optical, electrical, and dielectric properties of sprayed $NiFe_2O_4$ spinel-magnetic thin films", RSC Adv., Vol. 2, 10, 42, pp25143-25154

45. Shazzad Hossain, Md Emran Hossain, Shariful Islam, Md Rasel Rana, M. N. I. Khan, G. G. Biswas, Md Ashraf Ali and K. Hoque (2023), "Synthesis of Sr-doped $Ni_{0.5}Zn_{0.5}Sr_xFe_{2-x}O_4$ and the study of its structural, mechanical, magnetic, and electrical properties for high-frequency applications", Physics Open, Vol. 17, 100172

46. Salma Ikram, Fouzia Ashraf, Meshal Alzaid, K. Mahmood, N. Amin and S. Ali Haider (2023), "Role of Nature of Rare Earth Ion Dopants on Structural, Spectral, and Magnetic Properties in Spinel Ferrites", Journal of Superconductivity and Novel Magnetism, Vol. 34, 15, pp1-7

47. Mukhtar Ahmad, Muhammad Shahid, Yousef Mohammed Alanazi, Atiq ur Rehman, Muahmmad Asif and Charles W. Dunnill (2022), "Lithium ferrite ($Li_{0.5}Fe_{2.5}O_4$): synthesis, structural, morphological and magnetic evaluation for storage devices", Journal of Materials Research and Technology, Vol. 18, pp3386-3395

48. R. Verma, S. N. Kane, P. Tiwari, S. S. Modak and F. Mazaleyrat (2019), "Synthesis, Structural and Magnetic Properties of Cadmium Substituted Li-Ferrite", : AIP Conference Proceedings, Vol. 2142, 160006

49. Deepa Thapa, Nilesh Kulkarni, S. N. Mishra, P. L. Paulose and Pushan Ayyub (2010), "Enhanced magnetization in cubic ferrimagnetic $CuFe_2O_4$ nanoparticles synthesized from a citrate precursor: the role of Fe^{2+}", J. Phys. D: Appl. Phys., Vol. 43, 195004

50. A. V. Raut, R. S. Barkule, D. R. Shengule and K. M. Jadhav (2014), "Synthesis, structural investigation and magnetic properties of Zn2+ substituted cobalt ferrite nano particles prepared by the sol–gel auto-combustion technique", J. Magn. Mater., Vol. 358, 359, pp87–92

51. D. V. Kurmude, R. S. Barkule, A. V. Raut, D. R. Shengule and K. M. Jadhav (2014), "X-Ray Diffraction and Cation Distribution Studies in Zinc-Substituted Nickel Ferrite Nanoparticles", J Supercond Nov Magn, Vol. 27, pp547–553

52. S. K. Pradhan, S. Bid, M. Gateshki and V. Petkov (2005), Mater. chem. phys. Vol. 93, pp224-230

53. M. Yehia and S. M. Ismail (2014), "A. Hashhash, Structural and Magnetic Studies of Rare-Earth Substituted Nickel Ferrites", Journal of Superconductivity and Novel Magnetism, Vol. 27

54. C. Murugesan and G. Chandrasekaran (2015), "Impact of Gd^{3+} substitution on the structural, magnetic and electrical properties of cobalt ferrite nanoparticles", RSC Advances Vol. 5, pp73714-73725

55. S. N. Mathad, R. N. Jadhav, N. D. Patil and V. Puri (2013), "Structural and mechanical properties of Sr^{+2} doped bismuth manganite thick films", Int. J. Self-Propag. HighTemp. Synth., Vol. 22, 4, pp180–184

56. Carlos Arean, E. Diaz, J. Gonzalez and Maria Villa-Garcia (1988), "Crystal chemistry of cadmium-zinc ferrites. Journal of Solid State Chemistry", J Solid State Chem., Vol. 77, pp275-280

57. R. A. Pawar, M. Sunil, A. Patange, R. Shitre, S. K. Gore, S. S. Jadhav and S. E. Shirsath (2018), "Crystal chemistry and single-phase synthesis of Gd^{3+} substituted Co–Zn ferrite nanoparticles for enhanced magnetic properties", RSC Adv., Vol. 8, 25258

58. Santosh S. Jadhav, Sagar E. Shirsath, B. G. Toksha, S. M. Patange, S. J. Shukla And K. M. Jadhav (2009), "Structural properties and cation distribution of Co-Zn nano-ferrites", J. Mod. Phys. B, Vol. 23, 5629

59. Dipali S. Nikam, Swati V. Jadhav, Vishwajeet M. Khot, R. A. Bohara, Chang K. Hong, Sawanta S. Mali and S. H. Pawar (2015), "Cation distribution, structural, morphological and magnetic properties of $Co_{1-x}Zn_xFe_2O_4$ (x=0–1) nanoparticles", RSC Adv., Vol. 5, pp2338-2345

60. M. A. Amer and M. E. Hitti (2001), "Mossbauer and X-ray studies for $Ni_{0.2}Zn_xMg_{0.8-x}Fe_2O_4$ ferrites", J. Magn. Magn. Mater, Vol. 234, pp118–125

61. S. S. Desai, R. A. Pawar, S. S. Jadhav, Sagar E. Shirsath and S. M. Patange (2016), "Role of Coupling Divalent and Tetravalent Metal Ions on the Elastic and Electric Properties of $CoFe_2O_4$ Ferrites Prepared by Sol–Gel Method", Journal of Superconductivity and Novel Magnetism , Vol. 29, 10

62. Hemaunt Kumar, Jitendra Pal Singh, R. C. Srivastava, P. Negi, H. M. Agrawal, and K. Asokan (2014), "FTIR and Electrical Study of Dysprosium Doped Cobalt Ferrite Nanoparticles", Journal of Nanoscience Vol. 2014, 862415

63. Binu P Jacob, Ashok Kumar, R P Pant, Sukhvir Singh and E M Mohammed (2011), "Influence of preparation method on structural and magnetic properties of nickel ferrite nanoparticles", Bull. Mater. Sci., Vol. 34, 7, pp1345–1350

64. Matli Penchal Reddy, Xiobing Zhou, Aman Yann, Shiyu Du, Qing Huang, Adel Mohamed Amer Mohamed (2015), "Low-temperature hydrothermal synthesis, structural investigation and functional properties of $Co_xMn_{1x}Fe_2O_4$ (0≤x≤1.0) nanoferrites", Superlattices and Microstructures, Vol. 81, pp233-242

65. Sarwar Hasan and Bruska Azhdar (2022), "Synthesis of Nickel-Zinc Ferrite Nanoparticles by the Sol-Gel Auto-Combustion Method: Study of Crystal Structural, Cation Distribution, and Magnetic Properties", Advances in Condensed Matter Physics, Vol. 14, 4603855

66. Binu P Jacob, Ashok Kumar, R P Pant, Sukhvir Singh and E M Mohammed (2011), "Influence of preparation method on structural and magnetic properties of nickel ferrite nanoparticles", Bull. Mater. Sci., Vol. 34, 7, pp1345-1350

67. S. A. Mazen and N. I. Abu-Elsaad (2012), "Structural and some magnetic properties of manganese-substituted lithium ferrites", Journal of Magnetism and Magnetic Materials, Vol. 324, pp3366-3373

68. Sadiq. H. Khoreem, A. H. AL-Hammadi and W. F. Al-ryani (2023), "Investigation of Zn Substituted Ba-W-type Base Ferrites for FT-IR Structural and Vibrational Studies", Letters in Applied NanoBioScience, Vol. 12, 4, 164

69. Vinay Lakhani, T. Pathak, Nimish Vasoya, and Kunal Modi (2011), "Structural parameters and X-ray Debye temperature determination study on copper-ferrite-aluminates", Solid State Sciences, Vol. 13, pp539-547

70. Sadiq. H. Khoreem, A. H. AL-Hammadi and W. F. Al-ryani (2023), "Investigation of Zn Substituted Ba-W-type Base Ferrites for FT-IR Structural and Vibrational Studies", Letters in applied NanoBioScience, Vol. 12, 4, 164

71. Ch. Srinivas, E. Ranjith Kumar, B. V. Tirupanyam, Sher Singh Meena, Pramod Bhatt, C. L. Prajapat, T. V. Chandrasekhar Rao and D. L. Sastry (2020), "Study of magnetic behavior in co-precipitated Ni–Zn ferrite nanoparticles and their potential use for gas sensor applications", Journal of Magnetism and Magnetic Materials, Vol. 502, 166534

72. Mahwish Afzia, Rafaqat Ali Khan, Bushra Ismail, Magdi E. A. Zaki, Talal M. Althagafi, Abdulaziz A. Alanazi and Afaq Ullah Khan (2023), "Correlation between Magnetic and Dielectric Response of $CoFe_2O_4$:Li^{1+}/Zn^{2+} Nanopowders Having Improved Structural and Morphological Properties", Molecules, Vol. 28, 2824

73. Abhishek Nigam, Deepak Singh, Ankur Sinha, Deepak Sachan, Anisha, Ankur Vishal, Deepak Kumar and Naveen Kumar (2021), "Structural And Magnetic Properties Of Zinc Doped Nickel Ferrite $Ni_{(1-X)}Zn_xFe_2O_4$ Synthesized Using Sol-Gel Auto-Combustion And Hydrothermal Methods", Materials Physics and Mechanics, Vol. 47, pp493-500

74. V. S. Sawant and Keshav Rajpure (2015), "The effect of Co substitution on the structural and magnetic properties of lithium ferrite synthesized by an autocombustion method", Journal of Magnetism and Magnetic Materials Vol. 382

75. Hajar Jalili, Bagher Aslibeiki, Ali Ghotbi Varzaneh and Volodymyr A Chernenko (2019), "The effect of magneto-crystalline anisotropy on the properties of hard and soft magnetic ferrite nanoparticles", Beilstein J Nanotechnol, Vol. 10, pp1348-1359

76. A. S. Padam palle, B. K. Labde and N. M. More (2021), "High Field Magnetization, AC Susceptibility and Thermoelectric Power Studies of Pb^{4+} Substituted Nickel Ferrite", Our Heritage, Vol. 68, 12, pp527-533

77. Bashar Issa, Ihab M. Obaidat, Borhan A. Albiss, and Yousef Haik (2013), "Magnetic Nanoparticles: Surface Effects and Properties Related to Biomedicine Applications", Int J Mol Sci., Vol. 14, 11, pp21266-21305

78. Shitao Xu, Yongqing Ma, Bingqian Geng, Xiao Sun, and Min Wang (2016), "The remanence ratio in $CoFe_2O_4$ nanoparticles with approximate single-domain sizes", Nanoscale Res Lett., Vol. 11, 471

79. Abddaim Jeid, Mohamed Amghar, A. Mabrouki, A. Benali, A. Trabelsi, E. Dhahri, K. Khirouni and B. F. O. Costa (2023), "Study of physical properties of the $Li_{0.5}MgFe_{1.5}O_{3.5}$ ferrite nanoparticles", RSC Adv., Vol. 13, 19, pp12906-12916

80. Tetiana Tatarchuk, Mohamed Bououdina, Wojciech Macy, Olexander Shyichuk, Natalia Paliychuk, Ivan Yaremiy, Basma Al-Najar and Michal Pacia (2017), "Structural, Optical, and Magnetic Properties of Zn-Doped CoFe2O4 Nanoparticles", Nanoscale Research Letters, Vol. 12, 141

81. Yong Zhang (2018), "Electronic structures of impurities and point defects in semiconductors", Chinese Phys. B, Vol. 27, 117103

82. Mukhlis M. Ismail and Nasma A. Jaber (2018), "Dielectric properties of Li doped Ni-Zn ferrite", Iraqi Journal of Physics, Vol. 16, 36, pp140-152

83. Yendrapati Prabhu, Kalagadda Rao, Sesha Sai Kumar and Bandla Kumari (2014), "X-Ray Analysis by Williamson-Hall and Size-Strain Plot Methods of ZnO Nanoparticles with Fuel Variation", World Journal of Nano Science and Engineering, Vol. 04, pp21-28

84. Khalid Hellal Harbbi and Sarab Saadi Jahil (2017), "Study the Lattice Distortion and Particle Size of One Phase of MnO by Using Fourier Analysis of X-ray Diffraction Lines", Advances in Physics Theories and Applications, Vol. 65, pp6-22

85. Bantikatla Himabindu, N. S. M. P. Latha Devi and Bhogoju Rajini Kanth (2021), "Microstructural parameters from X-ray peak profile analysis by Williamson-Hall models; A review", Materials Today: Proceedings, Vol. 47, 14, pp4891-4896

86. Rakesh Vishwaroop and Shridhar N. Mathad (2020), "Synthesis, Structural, W-H Plot and Size-Strain Analysis of Nano Cobalt Doped $MgFe_2O_4$ Ferrite", Science of Sintering, Vol. 52, pp349-358

87. T. Jahanbin, M. Hashim, and K. A. Mantori (2010), "Comparative Studies on the Structure and Electromagnetic Properties of Ni-Zn Ferrites Prepared via Co-Precipitation and Conventional Ceramic Processing Routes", Journal of Magnetism and Magnetic Materials, Vol. 322, pp2684-2689

88. J. A. Allen (1968), "An Outline of Polymer Chemistry, Oliver and Boyd", Edinburgh, Vol. 25

89. M. A. Omar (1993), "Elementary Solid State Physics: Principles and Applications" Addison-Wesley, New York

90. H. P. Meyers and H. P. Myers (1997), "Introductory Solid State Physics. CRC Press", Boca Raton

91. B. D. Cullity (1978), "Elements of X-Ray Diffraction. Addison and Wesley Publishing Company Inc.", Reading, pp32-106

92. Y. M. Abbas, S. A. Mansour, M. H. Ibrahim and S. E. Ali (2011), "Microstructure characterization and cation distribution of nanocrystalline cobalt ferrite", J Magn Magn Mater, Vol. 323, pp2748-2756